



**QUEEN'S
UNIVERSITY
BELFAST**

Numerical investigation of dual-stage high velocity oxy-fuel (HVOF) thermal spray process: A study on nozzle geometrical parameters

Jafari, H., Emami, S., & Mahmoudi, Y. (2017). Numerical investigation of dual-stage high velocity oxy-fuel (HVOF) thermal spray process: A study on nozzle geometrical parameters. *Applied Thermal Engineering*, 111, 745-758. DOI: 10.1016/j.applthermaleng.2016.09.145

Published in:
Applied Thermal Engineering

Document Version:
Peer reviewed version

Queen's University Belfast - Research Portal:
[Link to publication record in Queen's University Belfast Research Portal](#)

Publisher rights
© Elsevier Ltd 2017. This manuscript version is made available under the CC-BY-NC-ND 4.0 license <http://creativecommons.org/licenses/by-nc-nd/4.0/> which permits distribution and reproduction for non-commercial purposes, provided the author and source are cited.

General rights
Copyright for the publications made accessible via the Queen's University Belfast Research Portal is retained by the author(s) and / or other copyright owners and it is a condition of accessing these publications that users recognise and abide by the legal requirements associated with these rights.

Take down policy
The Research Portal is Queen's institutional repository that provides access to Queen's research output. Every effort has been made to ensure that content in the Research Portal does not infringe any person's rights, or applicable UK laws. If you discover content in the Research Portal that you believe breaches copyright or violates any law, please contact openaccess@qub.ac.uk.

Numerical investigation of dual-stage high velocity oxy-fuel (HVOF) thermal spray process: a study on nozzle geometrical parameters

Hamed Jafari¹, Sobhan Emami^{1*}, Yasser Mahmoudi²

¹ Department of Mechanical Engineering, Najafabad Branch, Islamic Azad University, Najafabad, Iran.

² School of Mechanical and Aerospace Engineering, Queen's University Belfast, Belfast BT9 5AH, UK.

* Correspondence to

Tel.: +98 3142292383; Fax: +98 3142291016; Email: sobhan@pmc.iaun.ac.ir.

Abstract

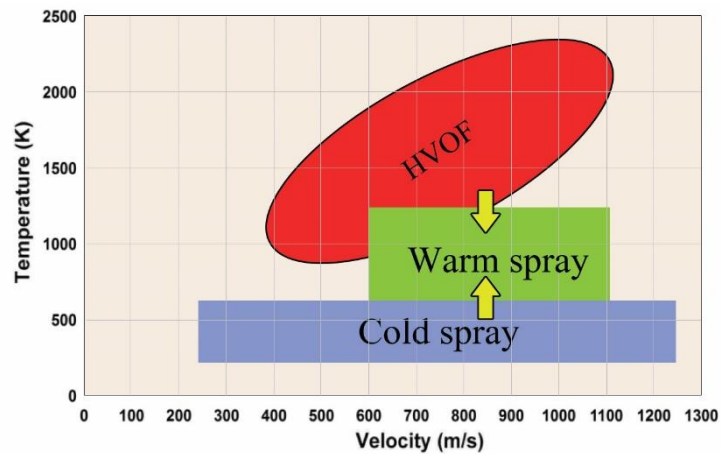
The present study takes the advantage of computational fluid dynamics (CFD) methods to model steady-state, two-dimensional, axisymmetric, turbulent, compressible and combusting flow in a dual-stage high velocity oxy-fuel (HVOF) thermal spray system. The Eulerian method is used to solve the continuum gas phase and the Lagrangian method is utilized for tracking the particles. The effects of particle loads on the continuous gas phase are included in the simulation. Thus, compared to the previous studies, we investigate the influence of coupling between the particle and gas phases in modeling of the dual-stage HVOF process. It is found that decouple modeling of the particle and the continuous phase causes a significant error in velocity of particle at the impact moment, even for low powder particle loading. We further investigate the effects of four geometrical parameters on the behavior of gas phase and consequently the particle phase. Results also show that the turbulent intensity of flow at different sections of the warm spray process is the most important factor determining the radial distribution of nitrogen and temperature in the barrel. It also determines the radial distribution of oxygen in the free jet outside of the barrel. It is further found that reduction of the first nozzle diameter and increasing the length of the divergent section (for a fixed divergent angle) of the convergent-divergent nozzle reduce the particle temperature while these changes do not affect the particle velocity. In other words, changing these geometrical parameters has a desirable effect on the particle temperature without causing an undesirable change on the particle velocity.

Keywords: thermal spray, dual-stage high velocity oxy-fuel (HVOF), coupled two-phase model, turbulent mixing, warm spray gun geometry.

1. Introduction

Engineering components are usually exposed to destructive environments, and coating is one of the most common and historical ways for protection of these components. Every component based on its mechanical performance and environment properties requires its own coating material and method. From all coating materials, titanium is an excellent coating material for different applications including biomedical implants [1, 2], off shore structures [3] and aerospace industry components [4]. The merit of titanium as a coating material nested in its high strength to weight ratio, corrosion resistance, biocompatibility and osseointegrate ability with living organisms [1, 4, 5-8]. Thermal spray techniques like high-velocity oxygen-fuel (HVOF) are common to be used for coating different metals.

41 Conventional single-stage HVOF thermal spray systems are typically a high pressure combustion
 42 chamber followed by a converging–diverging (C-D) nozzle. Injected particles are accelerated and
 43 heated through subsonic and then supersonic combusting gas flow and hit the substrate which is
 44 placed at around 300 mm from nozzle exit [9]. In order to form a layer of high quality coating,
 45 proper temperature and velocity at the impact moment need to be obtained [9]. HVOF has found
 46 to be one of the most efficient techniques to deposit high performance coatings at moderate cost
 47 [10]. However, HVOF system has no powerful control over the gas phase temperature and
 48 consequently the particle phase temperature. As it can be seen in Fig. 1, the particle temperature
 49 in HVOF system is above 900 K and it can go over 2000 K. Furthermore, in HVOF system,
 50 desirable change in temperature can cause an undesirable change in other characteristics. It is
 51 shown by Shamim et al. [11] that a decrease of reactant mass flow rate can cause a tiny desirable
 52 reduce in particle temperature but a drastic undesirable decrease in velocity. Moreover, decrease
 53 in fuel/oxygen ratio can reduce the temperature, instead produces unburned oxygen and hence
 54 increases coating oxide content [11].



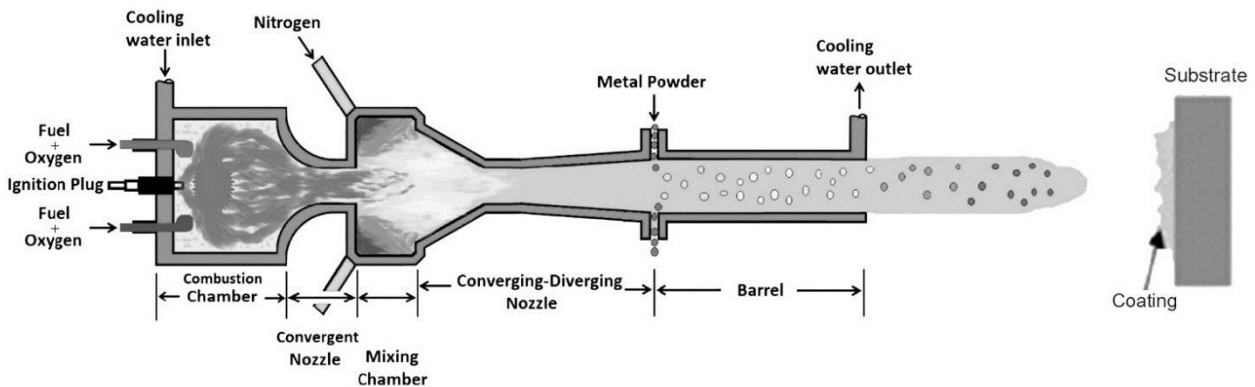
55

56 Fig. 1. Comparison of particle velocity and temperature in HVOF, cold spray and warm spray thermal spray
 57 processes [9] (published with permission).

58 Therefore, these limitations make single-stage HVOF thermal spray not a suitable coating method
 59 for phase-sensitive and temperature sensitive metals like titanium. Melting point of titanium is
 60 very low. It also has strong affinity toward oxygen and reacts with oxygen at relatively lower
 61 temperature compared to other materials [12]. Therefore, it is necessary to keep the temperature
 62 of titanium low since its oxidation rate increases exponentially when the particle temperature
 63 reaches to about 900 K [13]. Thus, using titanium in single-stage HVOF guns results in very low
 64 coating quality with high oxide content. One common titanium coating technique, which can
 65 control various detrimental reactions such as oxidation, is cold spray [14, 15]. As it is shown in
 66 Fig. 1, particle has low temperature in cold spray, and it hits the substrate while it is in the solid
 67 state. This coating system results in low deposition efficiency and high porosities within the
 68 coatings [16].

69 Dual-stage HVOF thermal spray system, which is also called warm spray, is introduced to fill the
 70 gap between the cold spray and single-stage HVOF spray processes [9]. Warm spray process
 71 inherits particle high momentum from cold spray and high temperature from HVOF spray.
 72 Titanium requires both of these characteristics (i.e. high velocity and controlled high temperature)
 73 in order to form dense, uniform, low oxide, well adhered and in one word high quality coatings.

74 Warm spray was first patented by Browning [17] and then developed by many researchers [18-
 75 21]. The principles of warm spray are similar to HVOF process. As can be seen in Fig. 2, a
 76 converging nozzle followed by a mixing chamber is placed between combustion chamber and C-
 77 D nozzle. In the mixing chamber different mass flow rates of nitrogen are added as coolant in order
 78 to dilute the hot gases. This can be known as the powerful temperature regulator in warm spray
 79 technique. Warm spray gun also has a barrel which joins to the C-D nozzle, and particles are
 80 introduced to the flow at the barrel entrance. Based on a study by Kuroda et al. [9], warm spray
 81 can maintain particle temperature in the range of 850-1400 K and particle velocity in the range of
 82 620-800 m/s. In such a range of velocity, the particle temperature in HVAF (high velocity air fuel)
 83 gun is between 1100-1300 K. In other words, Kuroda et al. [9] showed that the warm spray
 84 provides particle temperature three times wider than HVAF while maintaining the velocity
 85 comparable with it.



86
 87 Fig. 2. Schematic diagram of a warm spray process.

88 The processes in the thermal spray guns are very complex and involve multi-phase turbulent flow,
 89 chemical reaction, heat transfer and supersonic/subsonic flow transition [22]. Moreover, the
 90 influence of processing conditions on particle characteristics and coating quality is highly
 91 nonlinear and might not be thoroughly revealed by experimental studies [23]. Hence, numerical
 92 techniques are effective tools and can provide an insight into the underlying momentum and heat
 93 transfer mechanisms [24, 25]. This further helps to improve the efficiency of HVOF and warm
 94 spray coatings by optimizing all of the effective design parameters such as C-D nozzle geometry,
 95 fuel/oxygen ratio, particle size and so on [16, 23-31].

96 While many computational fluid dynamics (CFD) simulations have been done to investigate
 97 single-stage HVOF process, researches on the dual-stage HVOF are scarce. Tabbara et al. [3] were
 98 pioneered in performing numerical study on the modified HVOF gun. They studied the impact of
 99 nitrogen flow rate, nitrogen radial concentration in the barrel and particle trajectory on the particle
 100 temperature and velocity. It was concluded that increasing the rate of nitrogen leads to an increase
 101 of pressure in the upstream of C-D nozzle, and this intensifies the under-expansion of flow at
 102 nozzle outlet. They also found that in the near wall region, where the flow has lower temperature
 103 and lower axial velocity, the concentration of the nitrogen is more than central region. Moreover,
 104 it was deduced that smaller particles are more likely to get away from the centerline and move to
 105 the near wall region. Moreover, the importance of mixing between hot combustion gases and cold
 106 nitrogen on the performance of warm spray was emphasized in their paper [3]. Khan and Shamim
 107 [16] studied the effects of reactant and coolant mass flow rate and fuel/oxygen ratio on gas and

108 particle phases in a warm spray process. They [16] concluded that increasing the reactant mass
109 flow rate increases the particle temperature and velocity. It was further concluded that the highest
110 gas phase temperature occurs at stoichiometric mixture point while particle temperature increases
111 as the fuel/oxygen ratio increases [16]. More coolant flow rate reduces particle temperature and
112 increases the particle velocity only outside of the barrel [16]. Khan and Shamim [30] also
113 investigated the influence of some geometrical parameters in a dual-stage HVOF system and
114 reported that an increase in the combustion chamber diameter or length leads to a decrease in
115 temperature and velocity of particles. They [30] also reported that increasing the length of mixing
116 chamber leads to an increase in the gas phase residence time in the mixing chamber and results in
117 better mixing between the hot gases and nitrogen. It causes a significant decrease in the particle
118 temperature. Increase in the diameter of C-D nozzle exit, however, reduces the particle velocity
119 and increases its temperature [30].

120 The above literature review shows that mixing between hot gases and cold nitrogen is the most
121 sensitive factor and has significant effects on the gas dynamic and thermal behavior of flow in the
122 warm spray and consequently on the particle conditions (i.e. temperature and velocity). Therefore,
123 the aim of the present work is studying the nozzle geometry which mostly controls the mixing of
124 hot gases and nitrogen. The paper also visualizes the details of the flow properties in the
125 converging nozzle and C-D nozzle of a dual-stage HVOF. This provides an overview of the
126 sensitivity of the problem upon the geometry of the system. Hence, it highlights the regions in the
127 parametric space in which the choice of the nozzle geometry leads to an optimum design of a warm
128 spray. The current paper investigates the influence of four effective geometric parameters of dual-
129 stage HVOF gun. These parameters are (i) converging nozzle throat diameter, (ii) C-D nozzle
130 throat diameter, (iii) simultaneous changing of throat diameter of converging nozzle and C-D
131 nozzle and (iv) length of the divergent section of C-D nozzle. In addition, the previous numerical
132 studies considered low particle loading and assumed that the particle phase is decoupled from the
133 gas phase. Thus, another aim of the present work is to investigate the influence of coupling
134 between the particle phase and the gas phases in modeling of a dual-stage HVOF system. The
135 problem includes steady-state, axisymmetric flow calculations for turbulent, fully compressible,
136 high-speed and chemically combusting gas flow. The paper is organized as follows. In section 2
137 we provide the model development and the governing equations. Turbulence and combustion
138 models and the dynamics of the gas and particle phases are introduced in this section. In this
139 section we further give details on the numerical method, computational domain and boundary
140 conditions used to solve the governing equations. Section 3 presents the grid study and verification
141 of the results against previous studies. In section 4 the effect of coupling solution on the particle
142 dynamic is examined. In section 5 the results of the numerical modeling are presented and
143 discussed. In this section the effect of geometrical parameters of the nozzle are studied in detail.
144 Finally section 6 concludes the paper.

145 **2. Model development and mathematical formulation**

146 In the current study, the Eulerian formulation is used to solve the flow field and Lagrangian particle
147 tracking method is utilized to provide particle flow characteristics. The particle phase is coupled
148 with the gas phase, and the impact of particle loads on the gas phase is considered. The gas phase
149 problem contains mass, momentum and energy conservation equations along with turbulence and
150 equilibrium chemistry. The Eulerian method utilizes ideal gas assumption to deal with high speed,

151 compressible and Newtonian flow. Results from gas phase provides Lagrangian scheme with data
 152 to determine particle velocity, temperature and location. Since warm spray gun is completely
 153 axisymmetric, a two-dimensional domain is appropriate for computations.

154 To incorporate the effect of different physical phenomena involve in the problem, we used existing
 155 models in the literature. This is mainly due to the complexity of the multi-scale problem involving,
 156 compressible turbulent reactive phenomena with heat transfer, and modeling of C-D nozzle in a
 157 complicated geometry. Interaction between the continuum gas phase by solving Euler equation
 158 and tracking particle phase using Lagrangian method, adds more complexity to the problem.
 159 Therefore, we tried to utilize previous validated models to develop a validated modeling tool. This
 160 further allows us to have a quick model for the purpose of parametric and geometric studies that
 161 is the objective of the present work.

162 2.1. Gas phase dynamics

163 Viscous, compressible and turbulent flow in a warm spray gun is governed by the compressible
 164 reactive Navier–Stokes equations. This consists of balance equations for mass, momentum, energy
 165 and species. The ideal gas equation of state couples the pressure and density. The governing
 166 equations solved in this study are obtained by Favre (mass-weighted) averaging of transport
 167 equations. Therefore, the steady state continuity and momentum equations are written as:

$$\frac{\partial(\bar{\rho}\tilde{u}_j)}{\partial x_j} = 0, \quad (1)$$

$$\frac{\partial(\bar{\rho}\tilde{u}_j\tilde{u}_i)}{\partial x_j} = -\frac{\partial\bar{p}}{\partial x_i} + \frac{\partial}{\partial x_j} \left((\bar{\tau}_{ij})_{eff} \right) + S_{mom,p}, \quad (2)$$

$$(\bar{\tau}_{ij})_{eff} = \mu_{eff} \left(\frac{\partial\tilde{u}_i}{\partial x_j} + \frac{\partial\tilde{u}_j}{\partial x_i} \right) - \frac{2}{3}\mu_{eff} \frac{\partial\tilde{u}_l}{\partial x_l} \delta_{ij}, \quad (3)$$

168 where ρ is the density of gas, u_j is the j^{th} component of the gas field velocity, p is the static
 169 pressure, and μ_{eff} is the effective viscosity that is considered as the summation of the molecular
 170 viscosity, μ , and turbulent eddy viscosity, μ_t . Eddy viscosity is resulted from Reynolds stress terms
 171 and represents the effect of diffusing momentum. $(\bar{\tau}_{ij})_{eff}$ and δ_{ij} are the mean deviatoric stress
 172 tensor and the Kronecker symbol respectively. The superscripts (\sim) and $(-)$ denote a mass-
 173 weighted averaged quantity and a Reynolds averaged quantity.

174 In order to simulate two-way coupling, we need to consider the effect of particles on the
 175 momentum and energy equations of the continuous phase. Therefore, two terms appear as
 176 momentum and energy sinks in the continuous phase equations. For momentum equation (Eq. (2))
 177 the source term $S_{mom,p}$ is calculated as:

$$S_{mom,p} = -\frac{18 C_D \rho_g}{24 d_p} (\overline{U_g} - \overline{U_P}) |\overline{U_g} - \overline{U_P}|, \quad (4)$$

178 where ρ_g and d_p are the density of gas and diameter of particle, respectively. C_D , U_g and U_P are
 179 drag coefficient, gas phase velocity and particle phase velocity, respectively

180 The balance equations for energy and species are:

$$\frac{\partial}{\partial x_i} [\tilde{u}_i (\bar{\rho} \tilde{h}_t + \bar{p})] = \frac{\partial}{\partial x_j} \left[\left(\lambda + \frac{c_p \mu_t}{Pr_t} \right) \frac{\partial \tilde{T}}{\partial x_j} + \tilde{u}_i \left((\bar{\tau}_{ij})_{eff} \right) - \sum_{k=1}^{N_s} \bar{J}_k \tilde{h}_k \right] + S_{heat,p}, \quad (5)$$

$$\frac{\partial}{\partial x_j} (\bar{\rho} \tilde{Y}_k \tilde{u}_j) = - \frac{\partial}{\partial x_j} [\bar{J}_k] + \bar{\omega}_k; \quad k = 1, \dots, N_s - 1, \quad (6)$$

181 where T is the temperature, h_t is the total enthalpy obtained as $h_t = h + u_i u_i / 2$, λ is the thermal
 182 conductivity, Y_k is mass fraction of the species k and $\bar{\omega}_k$ is the mass reaction rate of species per
 183 unit volume. \bar{J}_k is the diffusion flux of a species k consists of molecular diffusion and effective
 184 diffusion due to turbulence. Pr_t is the turbulent Prandtl number that is estimated using Eq. (7)
 185 based on the RNG theory [32]:

$$186 \quad \left| \frac{\alpha - 1.3929}{\alpha_0 - 1.3929} \right|^{0.6321} \left| \frac{\alpha + 2.3929}{\alpha_0 + 2.3929} \right|^{0.3679} = \frac{\mu}{\mu_t}, \quad (7)$$

187 where μ is the molecular viscosity, μ_t is the turbulent eddy viscosity, $\alpha_0 = 1$, and $\alpha = 1/Pr_t$. The
 188 results that obtained from Eq. (7) for Pr_t is in close agreement with experimental data in a variety
 189 of flows [32]. This equation has also been used to investigate turbulent reactive flow in the single
 190 HVOF and dual stage HVOF (e.g. [16, 22, 26, 28, 30, 31, 43]). For single HVOF, turbulent
 191 properties of the flow predicted using Eq. (7), were in good agreement with experimental data
 192 [16]. In high Reynolds number, fully developed turbulence flow where μ/μ_t tends to zero, α
 193 becomes 1.3929 and the turbulent Prandtl number is $Pr_t = 0.7179$.

194 In Eq. (5) $S_{heat,p}$ is the energy sink in the energy equation of the continuous phase and is calculated
 195 by:

$$196 \quad S_{heat,p} = -\rho_p C_p \frac{dT_p}{dt}, \quad (8)$$

197 where ρ_p , C_p and T_p is density, specific heat at constant pressure and temperature of the particle,
 198 respectively.

199 2.1.1. Turbulence model

200 In this study the re-normalization group (RNG) k - ε model along with the non-equilibrium wall
 201 function treatment is used to predict the turbulent eddy viscosity. Since the nature of the flow in
 202 warm spray gun includes complex shear flows [30] with rapid strain and large pressure gradient,
 203 RNG k - ε is a stronger model in comparison with standard k - ε in order to predict turbulent core of
 204 the flow field [33]. This model provides good results for the core flow when the wall y plus is
 205 between 30 and 300 [33], which is satisfied in the current simulation. Nonetheless, it cannot solve
 206 the flow in the boundary layer accurately [33]. However, RNG k - ε is accurate enough to investigate
 207 the overall impacts of the geometrical parameters on the flow and particle field. In the RNG k - ε
 208 turbulence model the turbulent kinetic energy, k , and the rate of turbulent kinetic energy
 209 dissipation, ε , are expressed as follows:

$$\frac{\partial (\bar{\rho} \tilde{u}_j k)}{\partial x_j} = \frac{\partial}{\partial x_j} \left[\alpha_k (\mu + \mu_t) \frac{\partial k}{\partial x_j} \right] + G_k - \bar{\rho} \varepsilon - Y_M, \quad (9)$$

$$\frac{\partial (\bar{\rho} \tilde{u}_j \varepsilon)}{\partial x_j} = \frac{\partial}{\partial x_j} \left[\alpha_\varepsilon (\mu + \mu_t) \frac{\partial \varepsilon}{\partial x_j} \right] + \frac{\varepsilon}{k} (C_{1\varepsilon} G_k - \bar{\rho} C_{2\varepsilon} \varepsilon) - R_\varepsilon. \quad (10)$$

210

211 The constant values of the model in Eqs. (9) and (10) are $C_1 = 1.42$, $C_2 = 1.68$ and $C_\mu = 0.084$. α_k
 212 and α_ε are the inverse effective Prandtl numbers for k and ε . The production rate of turbulent kinetic
 213 energy, G_k , is written as:

214

$$G_k = \mu_t \left(\frac{\partial \tilde{u}_i}{\partial x_j} + \frac{\partial \tilde{u}_j}{\partial x_i} \right) \frac{\partial \tilde{u}_i}{\partial x_j} - \frac{2}{3} \left(\bar{\rho} k + \mu_t \frac{\partial \tilde{u}_i}{\partial x_i} \right) \frac{\partial \tilde{u}_k}{\partial x_k}, \quad (11)$$

215 where the turbulent eddy viscosity defined as $\mu_t = \bar{\rho} C_\mu k^2 / \varepsilon$.

216 2.1.2. Combustion model

217 The eddy dissipation model (EDM) developed by Magnussen and Hjertager [34] is the most
 218 common combustion model which is utilized in simulation of HVOF and warm spray guns (e.g.
 219 [16, 23, 24, 28, 30, 35, 36]). The EDM is based on the early eddy break-up combustion model
 220 (EBU) which was introduced by Spalding for the first time [37]. In these models, it is assumed
 221 that the reaction rate does not depend on chemical characteristics. As a consequence, the
 222 combustion rate is mostly controlled by the turbulent movements of the flow. In other words,
 223 turbulent flow breaks down eddies with fuel and oxidizer contents, and this process facilitates
 224 mixing. In the next step, the reactions are completed at the mixing moment. Therefore, these
 225 models are called infinite rate chemistry model or "mixed-is-burnt". Thus, these models are only
 226 suitable for problems with high Reynolds and Damkohler numbers (i.e. $Re \gg 1$ and $Da \gg 1$) where
 227 reaction time scale is much smaller than mixing time scale (which is estimated by k/ε) [38].

228 In the premixed combustion which happens in the problem of warm spray both fuel and oxygen
 229 exist in every single eddy and the minimum dissipation rate of fuel-oxidizer and products will
 230 appoint the reaction rate. In EDM, average concentration of species and the turbulent intensity in
 231 the flow are the only parameters which determine the reaction rate. Therefore, the volumetric fuel
 232 consumption rate is given by:

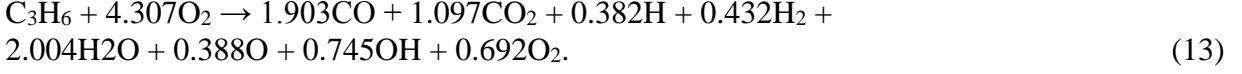
$$\bar{\omega} = -\bar{\rho} A \left(\frac{\varepsilon}{k} \right) \min \left(\tilde{Y}_F, \frac{\tilde{Y}_O}{S_O}, \frac{B \tilde{Y}_P}{1 + S_O} \right), \quad (12)$$

233 where $S_O = n_O M_O / n_F M_F$. A and B are constants taken as 4 and 0.5, respectively [38].

234 The Eddy Dissipation Model over-predicts the reaction rate in highly strained regions where ε/k
 235 ratio is high [38], and this can cause artificial flame to be observed. Moreover, for regions with
 236 similar species concentration and turbulence level but different temperatures, this model predicts
 237 similar reaction rate. To overcome these shortcomings, new finite rate chemistry combustion
 238 models, like eddy dissipation concept (EDC) model [39] and partially stirred reactor (PaSR) model
 239 [40] which consider the effects of chemical kinetics, are developed. It is unlikely that the
 240 weaknesses of EDM in comparison with the finite rate chemistry models mainly affect the major
 241 variables in the flow field and especially particle field. Nonetheless, the absence of a numerical
 242 investigation with detailed chemical kinetics in the HVOF system is still conspicuous, and it can
 243 be a topic for future researches.

244 Since the effect of chemical kinetics is ignored by EDM, the dissociation of major species should
 245 be considered in order to avoid the over-prediction of temperature. When combustion occurs, the

246 gauge pressure and temperature roughly reach to 3.5 bars and 2800 K in the base case (the
 247 geometry of the base case is introduced in Fig. 3). In such conditions using an instantaneous
 248 equilibrium model leads to the following chemical equation:



249 The stoichiometric coefficient of each species depends on the combustion chamber pressure and
 250 is not known a priori. Li and Christofides [28] used a trial and error method based on a one-
 251 dimensional (1-D) model along with a chemical equilibrium program (by Gordon and McBride
 252 [41]) to calculate the combustion pressure. They [28] showed that for different operating
 253 conditions leading to combustion pressures between 3 and 4.8 bars, the difference between
 254 calculated pressure from the above mentioned procedure and the experimental data is less than
 255 6%. In this work we used the data presented by Li and Christofides [28] for the chamber pressure.

256 2.2. Particle phase dynamics

257 The discrete phase model (DPM) takes the advantage of Lagrangian method to determine the
 258 particle motion and temperature using data coming from the gas phase momentum and heat
 259 transfer equations. It is assumed in previous studies [3, 11, 16, 27, 30, 42] that since the particle
 260 loading in the spray process is very low, the effect of particle dynamics on the continuous phase
 261 is minimal. Therefore, the particle phase can be decoupled from the gas phase. However, based on
 262 what will be discussed in section 4, decoupling the particle and the continuous phase will cause a
 263 remarkable error in prediction of the particle velocity at the impact moment.

264 It is also assumed that the particles do not affect each other. The particle is considered to be in a
 265 spherical shape and their motion is simulated by following equation [33]:

$$m_p \frac{d\vec{v}_p}{dt} = \frac{1}{8} \rho_g A_p C_D (\vec{U}_g - \vec{U}_p) |\vec{U}_g - \vec{U}_p| + \vec{F}, \quad (14)$$

266 where C_D , U_g and U_p are drag coefficient, gas phase velocity and particle phase velocity,
 267 respectively. Also A_p is the surface area of the particle.

268 While the roughness and orientation of particle surface are important, the particle Reynolds
 269 number (Re_p) is the dominant parameter on the drag coefficient [10]. Thus, the following equations
 270 define particle drag coefficient and Reynolds number respectively [33].
 271

$$C_D = \left\{ \begin{array}{l} \frac{24(1+0.15Re_p^{0.687})}{Re_p}, Re_p \leq 10^3 \\ 0.44, Re_p > 10^3 \end{array} \right\}. \quad (15)$$

$$Re_p = \rho_g \frac{|\vec{U}_g - \vec{U}_p|}{\mu_g} d_p. \quad (16)$$

272 Since the particle Biot number is less than 0.1 [43] the particles internal resistance is ignored and
 273 the temperature gradient inside the particle is assumed to be zero. For the base case, we studied
 274 the effect of radiation by using the Discrete Ordinate (DO) radiation model. The results predicted
 275 for the radiative model are similar to the non-radiative model. Therefore, the effect of radiation is

276 ignored for the rest of the cases studied in this paper. Thus, the heat transfer equation between a
 277 single particle and continuous gas phase is described as:

$$m_p C_p \frac{dT_p}{dt} = A_p h_c (T_g - T_p), \quad (17)$$

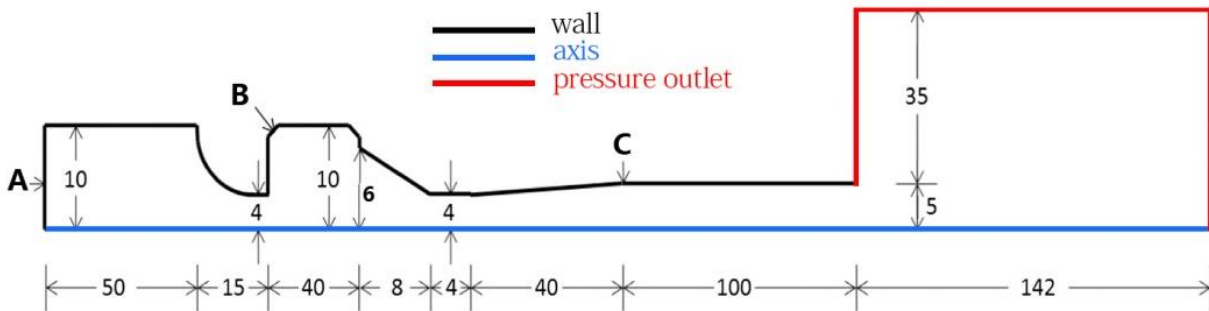
278 where h_c is the convection coefficient obtained as $h_c = Nu \lambda_g / d_p$. Nu is the Nusselt number
 279 defined by Ranz and Marshall correlation [44] as $Nu = 2.0 + 0.6Pr^{0.33} Re_d^{0.5}$ and λ_g is the thermal
 280 conductivity of the gas phase. Pr also is laminar Prandtl number of the continuous phase defined
 281 as $c_p \mu / \lambda_g$.
 282

283 2.3. Numerical method

284 We utilized the CFD commercial code ANSYS Fluent 16.1 to solve the governing equations. The
 285 solver performs under 2-D, axisymmetric, double precision, steady-state and pressure based
 286 conditions. The pressure and density are connected using the ideal gas state equation. Semi-
 287 Implicit Method for Pressure Linked Equations (SIMPLE) algorithm [45] is employed to treat
 288 pressure-velocity coupling. SIMPLE algorithm is commonly used in modeling high speed
 289 combusting flow in HVOF guns [16, 26, 30, 35, 36]. Since the radial distribution of nitrogen,
 290 oxygen and temperature is studied in this paper, the second order upwind discretization approach
 291 is utilized for all equations in order to avoid numerical diffusion.

292 2.4. Computational domain and boundary conditions

293 The schematic diagram and the boundary conditions of a warm spray gun are shown in Fig. 3. The
 294 computational domain includes combustion chamber, converging nozzle, mixing chamber, C-D
 295 nozzle, barrel and finally atmosphere (where the substrate is located). A, B and C indicate inlets
 296 for fuel-oxygen, nitrogen and particle, respectively.



297
 298 Fig. 3. Schematic diagram and boundary conditions of a typical warm spray gun. Dimensions are in mm for the base
 299 case.

300 The main objective in the present work is to examine the effect of the nozzle geometry (i.e.
 301 converging nozzle and C-D nozzle) on the gas flow and particle behavior in the warm spray. To
 302 do this, we consider the change of four effective geometric parameters. These are (i) changing
 303 throat diameter of the converging nozzle, (ii) changing the throat diameter of the C-D nozzle, (iii)
 304 simultaneous changing of the throat diameter for both converging and C-D nozzles and (iv) length
 305 of the C-D nozzle divergent section. This generates 13 geometrical cases which are analyzed
 306 numerically in this paper. Table 1 presents the variable dimensions for these 13 cases. Table 2 also
 307 presents the working conditions of warm spray. All wall temperatures are fixed at 350 K, and the

308 entrance temperature of fuel-oxygen, nitrogen and particle is assumed to be 300 K [30]. The
 309 ambient pressure is also fixed at 1 atm. The particle diameter is 15 μm and other particle properties
 310 are taken from Ref. [30].

311 Table 1. Description of 13 studied cases. The inlet diameter and the divergent angle of the 2nd nozzle are fixed
 312 at 12mm and 1.47°, respectively.

Variable case	1 st nozzle throat diameter	2 nd nozzle throat diameter	length of the 2 nd nozzle divergent portion
Base case	8mm	8mm	40mm
1 st Group Case 1 Case 2 Case 3	6mm 7mm 9mm	8mm	40mm
2 nd Group Case 4 Case 5 Case 6	8mm	6mm 7mm 9mm	40mm
3 rd Group Case 7 Case 8 Case 9	6mm 7mm 9mm	6mm 7mm 9mm	40mm
4 th Group Case 10 Case 11 Case 12 Case 13	8mm	8mm	30mm 35mm 45mm 50mm

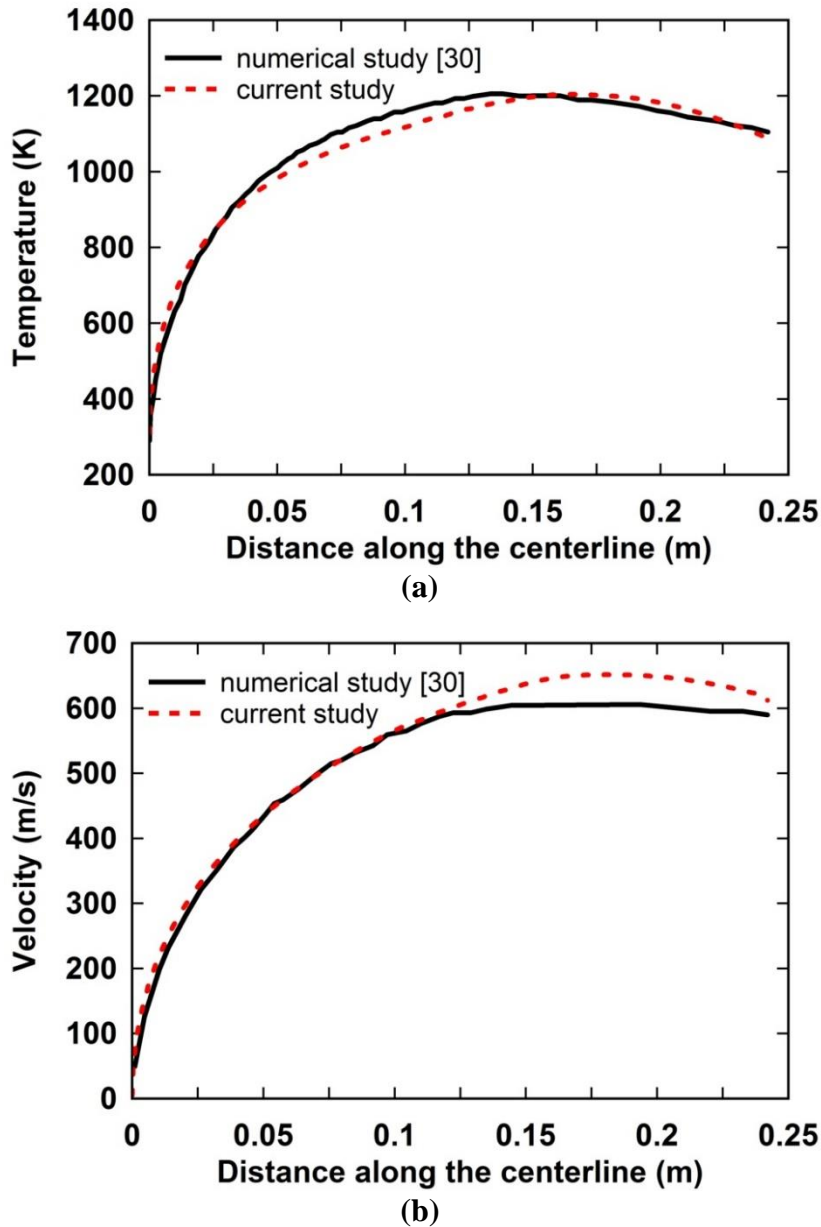
313 Table 2. Operating conditions.

parameter	value
Fuel + Oxygen mass flow rate	0.008740 kg/s
Nitrogen mass flow rate	0.008604 kg/s
Particle mass flow rate	0.000668 kg/s

314 3. Grid study and verification of the results

315 In order to conduct the grid independency test we study the effect of grid resolution on the variation
 316 of velocity on the centerline. Velocity is an important and sensitive variable in the warm spray
 317 gun, and it is important to make sure that this variable is not affected by grid resolution. Hence,
 318 three grids with 14100, 54760 (taken from Khan and Shamim [30]) and 129420 cells are used to
 319 study the grid independency. Our analysis reveals that grid with 14100 cells provided results with
 320 non-physical fluctuations mainly in the barrel. However, results for a grid with 54760 cells are
 321 completely logical and the difference between the gas phase velocity for grids with 54760 and
 322 129420 cells is less than 3%. It should be mentioned that the percentage of error for the velocity
 323 of particle phase is much less than those obtained for the gas phase. Thus, the grid with 54760
 324 cells is utilized for the rest of the computations.

325 For validation purposes, the computed temperature and velocity of the particle phase are compared
 326 to those of Khan and Shamim [30]. Fig. 4 depicts a good agreement between the present numerical
 327 results with those of Ref. [30].



328 Fig. 4. Comparison of (a) temperature and (b) velocity of the particle phase as a function of distance along the
 329 centerline obtained in the present work against the numerical results of Ref. [30].

330 4. Effect of coupled solution on the particle properties

331 In a study by Yang and Eidelman [42], it is commented that since the particle mass flow rate is
 332 less than 4% of continuous phase mass flow rate, the effect of particle loading on the continuous
 333 phase is minimal. Therefore, the momentum and heat exchange from particle to the gas phase can
 334 be neglected and the particle phase can be decoupled from the gas phase. This approach was used
 335 to simulate particle motion and temperature in several numerical investigations of HVOF and
 336 warm spray guns (e.g. [3, 11, 16, 27, 30, 42]). To examine this assumption, the current study
 337 considers the effect of interphase momentum and heat exchange on the particle phase behavior.
 338 The results are presented in Figs. 5 and 6. The effect of coupled solution and particle loading on
 339 the particle temperature and velocity is shown in Fig. 5. The particles enter the gun at the barrel
 340 entrance and path along the centerline until reach to the end of the computational domain. Also,
 341 Fig. 6 displays the effect of particle loading on the particle temperature and velocity at barrel exit.

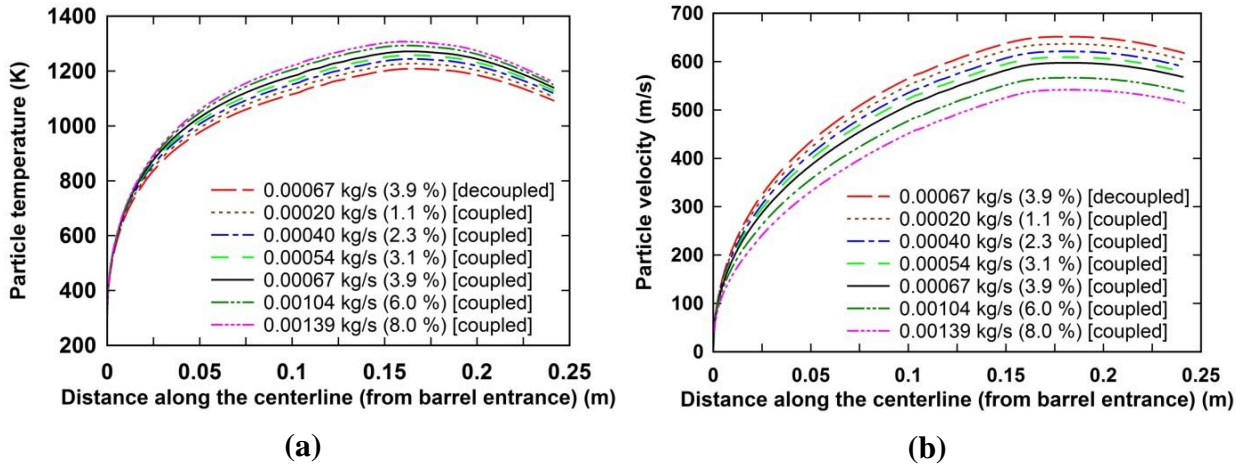


Fig. 5. Effect of particle mass flow rate on the particle (a) temperature and (b) velocity.

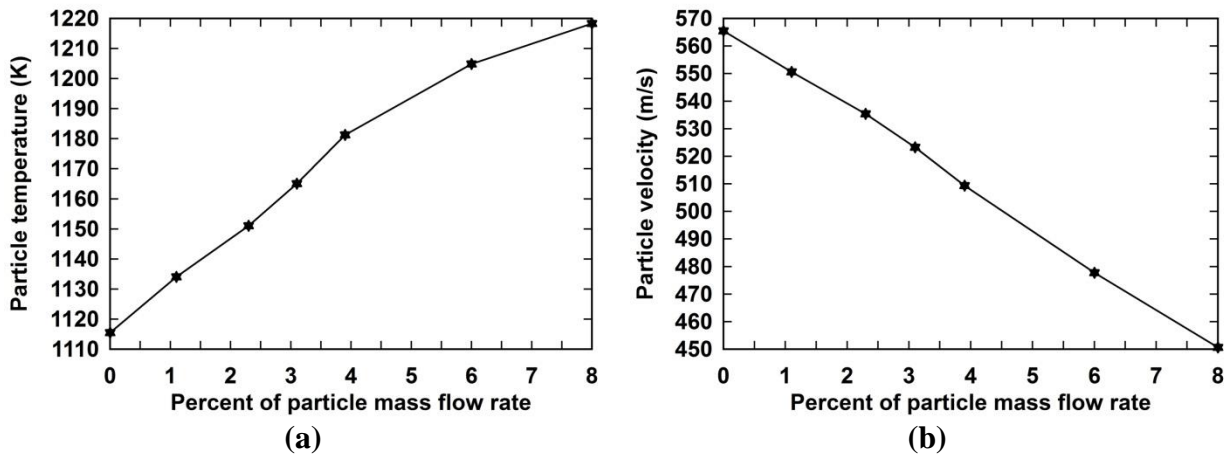


Fig. 6. Effect of particle mass flow rate on the particle (a) temperature and (b) velocity at barrel exit.

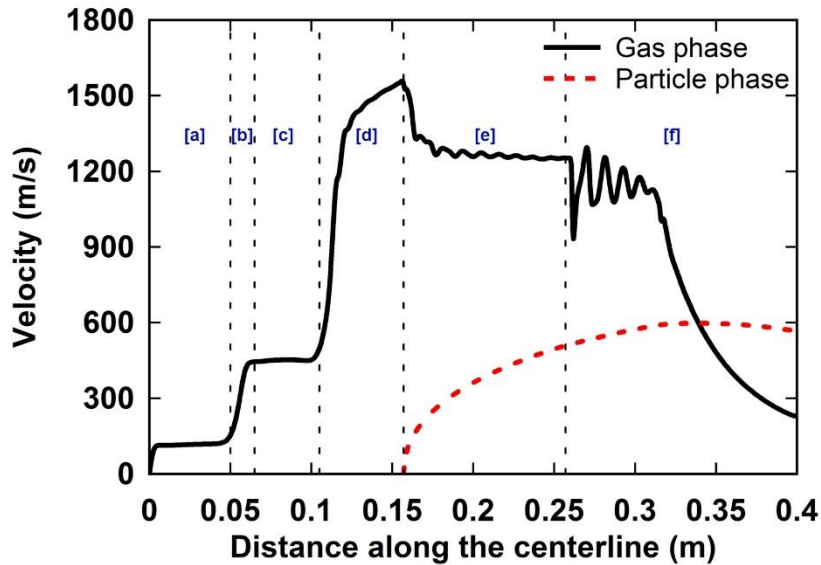
342 These figures reveal two important facts about the interaction between the two phases. Firstly, Fig.
 343 6 shows that for percent of particle mass flow rate lower or higher than 3.9%, the velocity and
 344 temperature of the particle have a linear dependency to the percent of particle mass flow rate. It
 345 seems that the 4% particle loading is not an exact criterion for decoupling particle and gas dynamic.
 346 Secondly, as it is seen in Figs. 5 (a) and 6 (a), for a fixed particle mass flow rate (i.e. 3.9%) the
 347 particle temperature at barrel exit predicted using decoupled solution is almost 5% lower than that
 348 obtained for a coupled solution. Moreover, Figs. 5 (b) and 6 (b) show that at the barrel exit, the
 349 particle velocity based on the decoupled solution is almost 10% higher than that of the coupled
 350 solution. This further clarifies the role of coupled solution in accurate molding of flow in the warm
 351 spray. Thus, in the present work the effect of particle on the continuous phase is considered for all
 352 cases studied.

353 5. Results and discussion

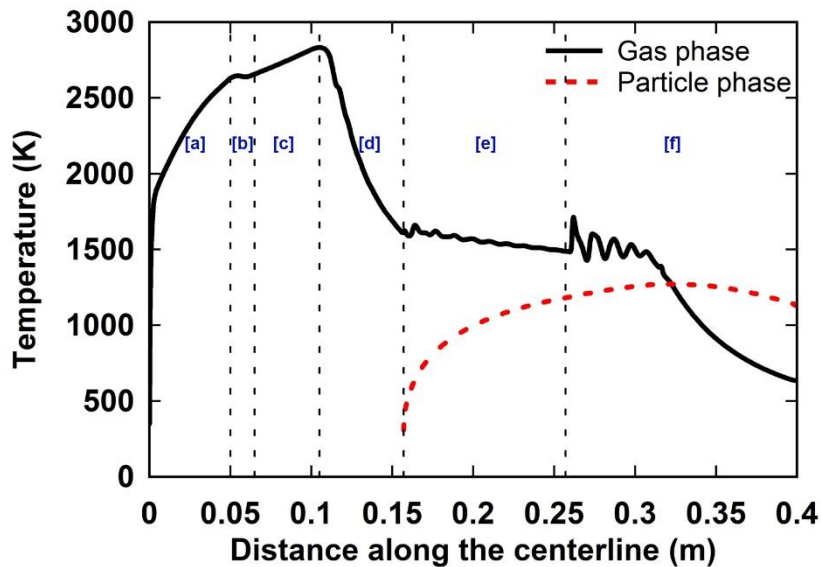
354 5.1. Analysis of gas dynamic and particle behavior

355 Fig. 7 shows the variation of velocity and temperature of the particle and gas phases along the
 356 centerline which is obtained for the base case given in Table 1. In warm spray system the

357 combustion chamber temperature increases due to combustion process. This high level of internal
 358 energy converts to kinetic energy when the exhaust gases accelerate through a converging nozzle.
 359 It can be seen in Fig. 7(a) that the flow experiences 350 m/s increase in velocity when it passes
 360 through the converging nozzle. By the next step, nitrogen is added to flow in mixing chamber to
 361 cool down the flow. In this stage, velocity and pressure remain roughly constant on the centerline,
 362 but the increasing rate of temperature decreases. Then, in C-D nozzle, the flow accelerates and
 363 becomes supersonic. Therefore, the flow experiences a drastic decline in pressure and temperature.



(a)



(b)

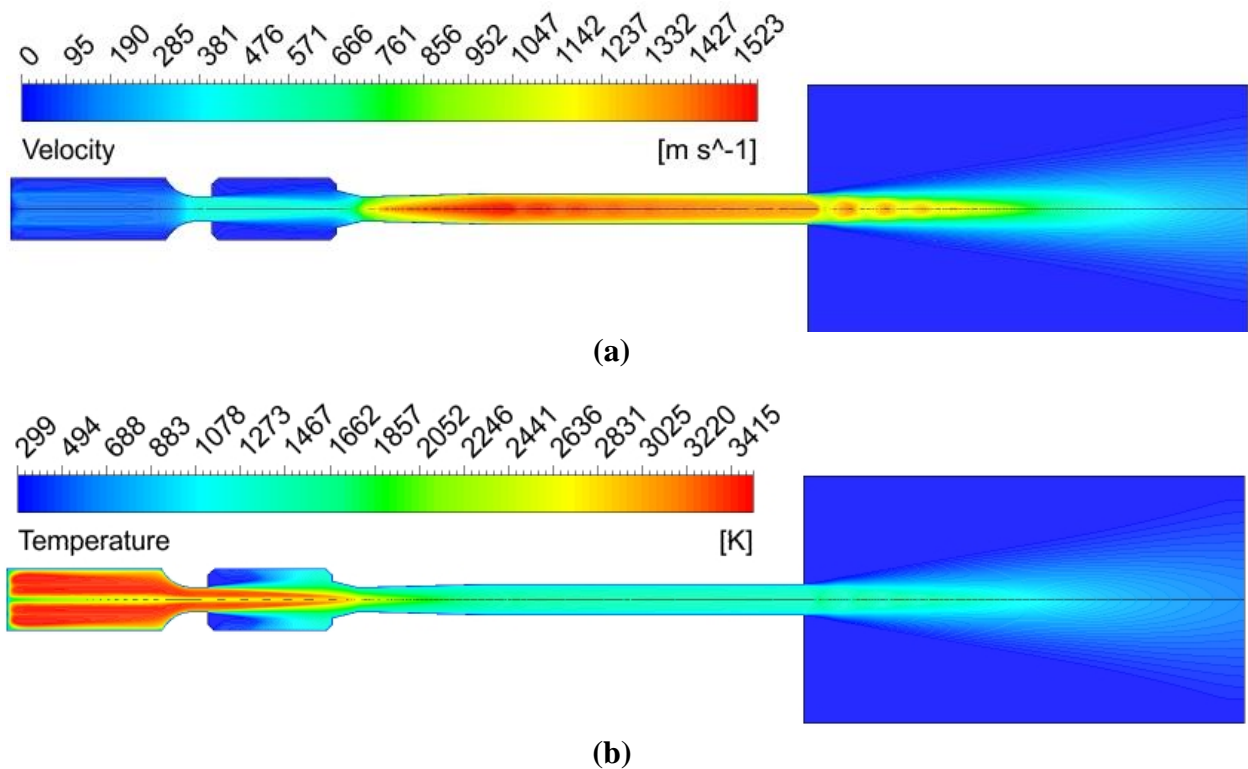
364 Fig. 7. Distribution of (a) velocity and (b) temperature as a function of distance along the centerline obtained for the
 365 base case for gas phase (solid line) and particle phase (dotted line). [a], [b], [c], [d], [e] and [f] indicate combustion
 366 chamber, converging nozzle, mixing chamber, C-D nozzle, barrel and outside atmosphere, respectively.

367 Fig. 8 presents the contours of velocity and temperature in the computational domain. It is seen
 368 when the supersonic flow enters the barrel, it passes through a series of incident and reflected
 369 oblique shock waves. This shock structure results in the small fluctuations in velocity and
 370 temperature in the barrel as can be seen in Fig. 7. However, both velocity and temperature remains

371 almost constant through the barrel (Fig. 7). When the flow comes out of the barrel, the exhaust
 372 supersonic jet has a boundary surface which interfaces with the surrounding quiescent atmospheric
 373 air [46]. This free boundary reflects an incident shock wave as an expansion wave and vice versa.
 374 Therefore, the diamond-like wave patterns with compression and expansion waves form at
 375 downstream of the barrel exit. This complicated structure causes the gas velocity and temperature
 376 to undergo a series of fluctuations as seen in Fig. 7.

377 It is further seen in Fig. 7 that the velocity and temperature of the particle phase increase drastically
 378 along the centerline up to $x = 0.20$ m. Then a monotone increase in the particle velocity and
 379 temperature are observed up to $x = 0.34$ m and $x = 0.32$ m, respectively. It means that the particle
 380 obtains its peak temperature and velocity outside of the gun. These maximum values for the base
 381 case are 597.5 m/s and 1271.7 K. Then slight decreases in these properties are observed until the
 382 exit of the computational domain. After the particle reaches to its peak temperature, the direction
 383 of heat transfer changes, and heat transfers from the particle to the gas flow.

384 From Fig. 7 (a) it is obvious that when the particles are injected to the gun (i.e. barrel entrance),
 385 the gas velocity decreases sharply. This behavior was not observed in the previous simulations of
 386 warm spray process (e.g. [16, 30]). This can be attributed to the interaction between particle and
 387 flow in a two-way coupling manner.



388 Fig. 8. Contour of (a) velocity and (b) temperature of the gas phase for the base case.

389 The following sections discuss the effect of four important geometrical design parameters on the
 390 performance of the warm spray guns.

391 5.2. Effect of converging nozzle throat diameter

392 Fig. 9 shows the effect of throat diameter of the converging nozzle on the gas and particle phases'
393 properties. According to Table 1, Case 1 and Case 2 have 1st nozzle throat diameters smaller than
394 the base case while Case 3 has a diameter higher than the base case. Fig. 9 shows that the throat
395 diameter of 1st nozzle does not have significant effect on the flow velocity and temperature
396 upstream of the nozzle while it causes remarkable changes on the flow in the downstream of the
397 nozzle. Up to $x = 0.157$ m (the barrel entrance), the gas phase velocity is affected by the nozzle
398 throat diameter. Reduction of the first nozzle diameter increases the pressure in the combustion
399 chamber, and reduces the pressure and increases the gas velocity in the mixing chamber. In
400 contrast, this change does not affect these variables in the barrel since the stagnation pressure in
401 the mixing chamber is the same for all cases. Therefore, the gas velocity in the barrel does not
402 change with the throat diameter while the gas temperature experiences noticeable changes. Since
403 the flow velocity and pressure at barrel exit are almost equal for all cases, the diamond-like jets at
404 barrel exit, which are visible as fluctuations in Fig. 9, look similar. Fig. 9 shows that increasing
405 the 1st nozzle throat diameter has no remarkable effect on the particle velocity while this change
406 has a substantial effect on the particle temperature. It can be concluded that the behavior of the gas
407 properties have the same effects on the particle properties. It is an interesting finding that changing
408 the diameter of converging nozzle serves a powerful control over the particle temperature while
409 the particle velocity remains intact. Based on the results presented in Fig. 9 (b), 33% decrease in
410 the nozzle throat diameter (comparison between Case 1 and Case 3) causes 11% decline in the
411 particle temperature at the end of the computational domain. The decrease in the gas phase and
412 particle temperature is due to the fact that by reducing the diameter of converging nozzle the
413 turbulent behavior of flow in the mixing chamber and C-D nozzle increases. This enhances the
414 turbulent mixing of hot gases and cold nitrogen.

415 To evaluate of the effect of turbulent mixing, the variation of the turbulent intensity along the
416 centerline is given in Fig. 10 for all above cases. As it is seen, Case 1 (related to minimum nozzle
417 diameter) has the highest level of turbulent intensity in the mixing chamber and C-D nozzle. For
418 this case, the turbulent intensity increases due to a stronger jet-like flow which passes through the
419 converging nozzle resulting in a more strained shear layer. The increase of turbulent intensity
420 enhances the turbulent mixing of hot combustion products and nitrogen cooling gas.

421 To show the effect of turbulent mixing on the radial diffusion of nitrogen, the radial distribution
422 of N_2 mole fraction at the barrel entrance (the location of particle injection) is presented in Fig. 11
423 (a). It is seen that the radial distribution of N_2 in Case 1 is more uniform at barrel entrance. It means
424 that the higher level of turbulent mixing can lead to an increase of radial diffusion of nitrogen.
425 Also, the cooling effect of nitrogen results in a more uniform distribution of radial temperature.
426 The uniform radial distribution of temperature shows its practical importance when the particles
427 get away from the centerline. The radial distance of particle from the centerline determines the
428 degree of heating and melting of the particles. As the particles get away from the centerline, their
429 temperature decreases [3]. In fact, a radial uniformity in gas phase temperature results in an
430 uniformity of the particle temperature regardless of particles' radial distance from the centerline.

431 The effect of throat diameter of the 1st nozzle on the variation of radial O_2 distribution at 63 mm
432 outside of barrel (i.e. $x = 320$ mm where the particles typically attain their highest temperature) is
433 depicted in Fig. 11 (b). In practice, radial distribution of oxygen determines the oxidant content of
434 particles at the point of impact on the substrate and consequently the coating quality. It can be seen

435 that the radial O₂ distributions are the same for all cases. The oxygen content of the jet flow in the
 436 atmosphere is mostly resulted from jet velocity at barrel exit because the flow with higher velocity
 437 at barrel exit faces higher turbulent intensity and higher turbulent mixing with ambient air.
 438 Therefore, roughly same velocity at barrel exit (Fig. 9 (a)) leads to the same level of turbulent
 439 intensity (Fig. 10) and radial oxygen content (Fig. 11 (b)).

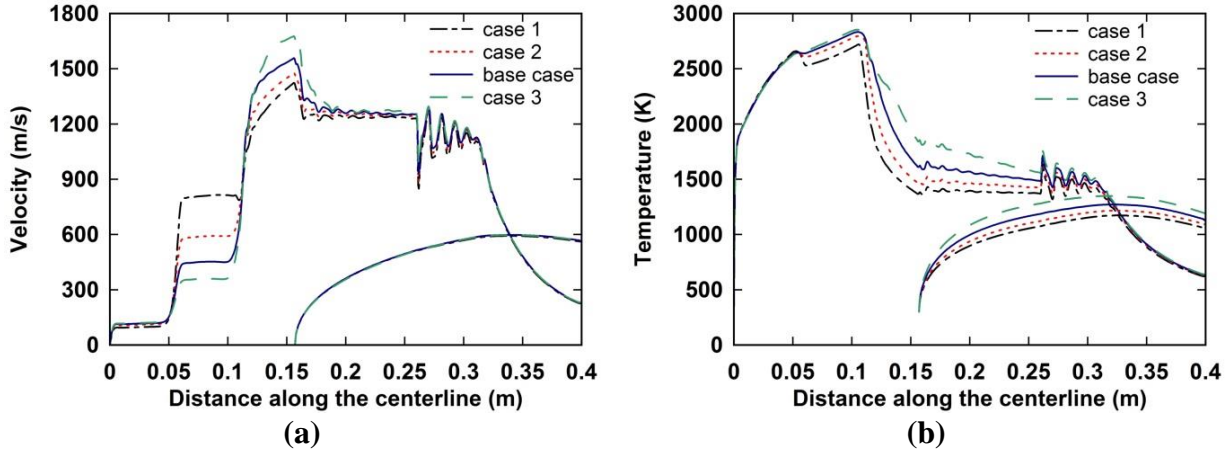


Fig. 9. Effect of throat diameter of the 1st nozzle on the variation of (a) velocities and (b) temperatures of the gas and particle phases along the centerline.

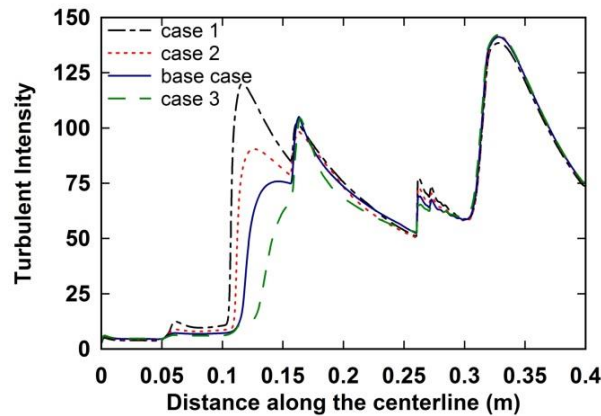


Fig. 10. Effect of throat diameter of the 1st nozzle on the variation of turbulent intensity of flow along the centerline.

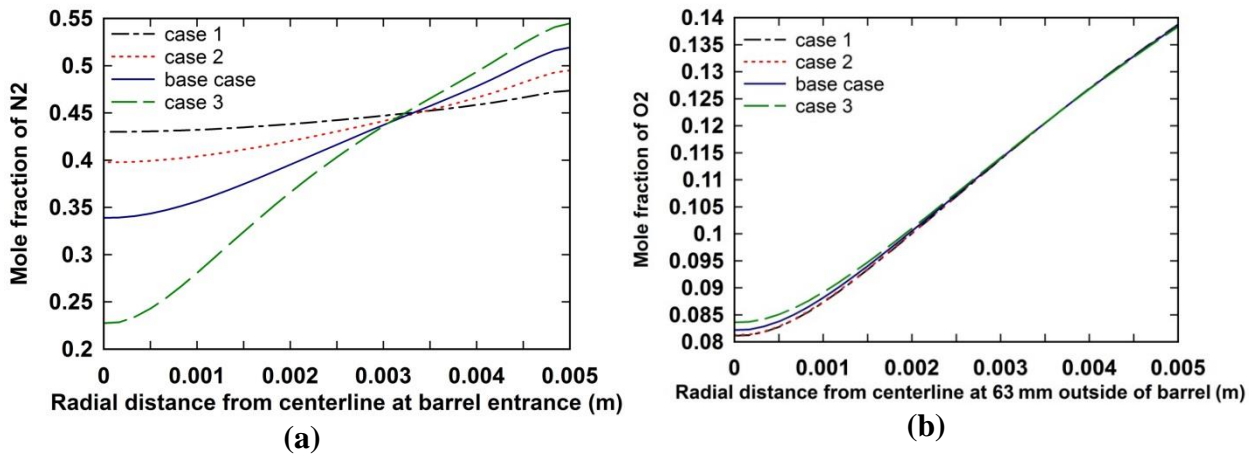


Fig. 11. Effect of throat diameter of the 1st nozzle on the variation of (a) nitrogen radial distribution at the barrel entrance and (b) oxygen radial distribution at 63 mm outside of the barrel (i.e. $x=320$ mm).

440 5.3. Effect of C-D nozzle throat diameter

441 The impact of C-D nozzle throat diameter in a liquid-fueled single stage HVOF gun was studied
442 by Tabbara et al. [44]. The current paper studies the impact of this parameter in a gas-fueled warm
443 spray. Fig. 12 presents the velocity and temperature of gas and particle phases due to a change in
444 the throat diameter of the second nozzle. According to Table 1, Case 4 and Case 5 have 2nd nozzle
445 throat diameters smaller than the base case while Case 6 has a diameter higher than the base case.
446 Changing this parameter does not affect the flow velocity upstream of the throat in the single-stage
447 HVOF gun. This was observed in the study by Tabbara et al. [44]. Nonetheless, changing the 2nd
448 nozzle throat diameter has remarkable effect on the upstream velocity of gas, especially in the
449 mixing chamber. As it can be seen in Fig. 12 (a), decrease in C-D nozzle throat diameter results in
450 a reduction of gas velocity in the combustor and mixing chamber. Similar to the single stage, in
451 the dual stage HVOF, a decrease in C-D nozzle throat increases gas velocity and consequently the
452 particle velocity in the downstream of the nozzle throat. An increase of the throat diameter reduces
453 the stagnation pressure in the mixing chamber. Thus, further increase in the throat diameter (i.e.
454 Case 6 in Table 1) causes the flow to expand normally through the nozzle and barrel. This is why
455 no shock structure is seen in Fig. 12 (a) at the barrel exit (dashed green lines in Figs. 12 (a) and
456 (b)).

457 From Fig. 12 (b) it is obvious that by increasing the C-D nozzle diameter, the particle temperature
458 increases from Case 4 to Case 6. The particle temperature is influenced by the gas phase
459 temperature and the residence time of particles in the barrel. Therefore, the increase in the particles
460 temperature from Case 4 to Case 6 is due to both higher gas phase temperature and lower particle
461 velocity (i.e. higher residence time). Based on Fig. 12 (b), 33% decrease in the nozzle throat
462 diameter (going from Case 4 to Case 6) causes 10% decline in the particle temperature and 9%
463 decline in the gas temperature at the end of the computational domain.

464 Fig. 13 shows the effect of C-D nozzle throat diameter on the turbulent intensity of the flow. As it
465 is mentioned above, the level of turbulent intensity in the mixing chamber and C-D nozzle
466 determines the radial distribution of nitrogen, and consequently, distribution of temperature in the
467 barrel. Compared to the other cases, the turbulent intensity of Case 6 in mixing chamber and C-D
468 nozzle is the highest one. Therefore, in this case the radial distribution of nitrogen (see Fig. 14 (a)),
469 and consequently, the temperature distribution is more uniform. Also the oxygen content of flow
470 outside the barrel is influenced by the turbulent intensity caused by the jet velocity. Therefore, as
471 it is seen in Fig. 14 (b), the highest oxygen content at this region occurs in Case 4 with the highest
472 jet velocity at barrel exit. This increases the peril of oxidation in this case. In a study by Tabbara
473 et al. [44], it was found that 20% reduction in C-D nozzle throat of single stage HVOF resulted in
474 60% increase in the pressure of combustion chamber. The current work shows that 20% decline in
475 C-D nozzle throat causes 65% increase in gauge pressure of the combustion chamber. Hence, the
476 impact of C-D nozzle throat diameter on combustion chamber pressure for single and dual HVOF
477 is the same.

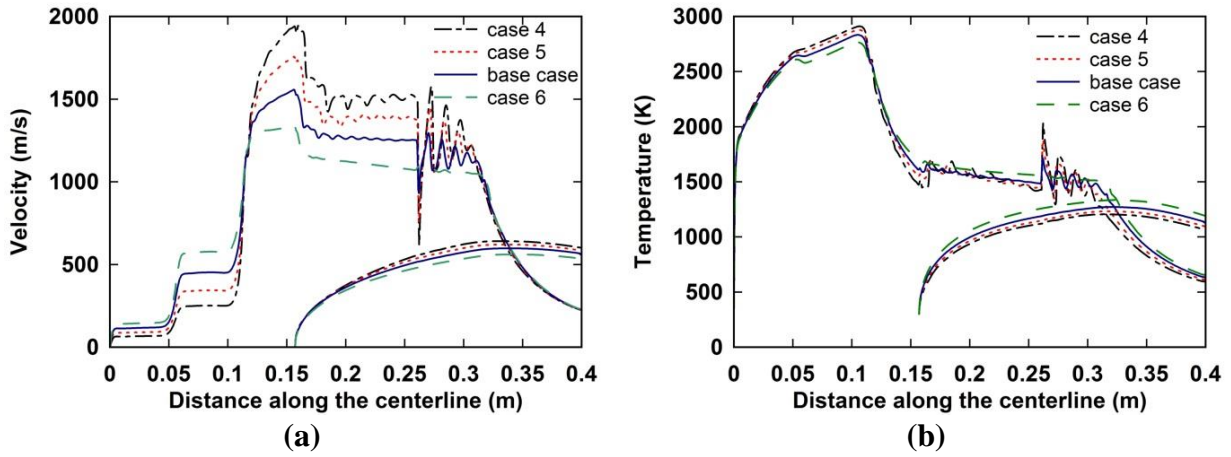


Fig. 12. Effect of throat diameter of the 2nd nozzle on the variation of (a) velocities and (b) temperatures of the gas and particle phases along the centerline.

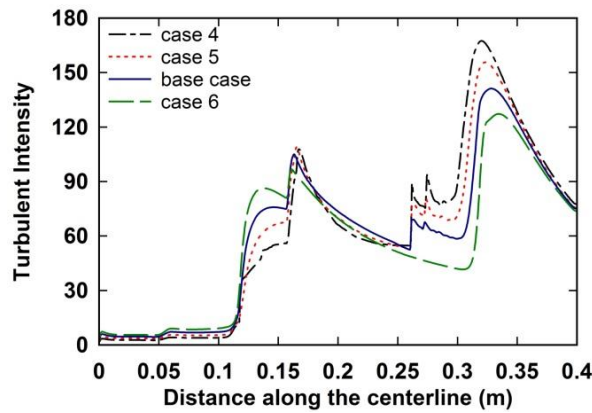


Fig. 13. Effect of throat diameter of the 2nd nozzle on the variation of turbulent intensity of flow along the centerline.

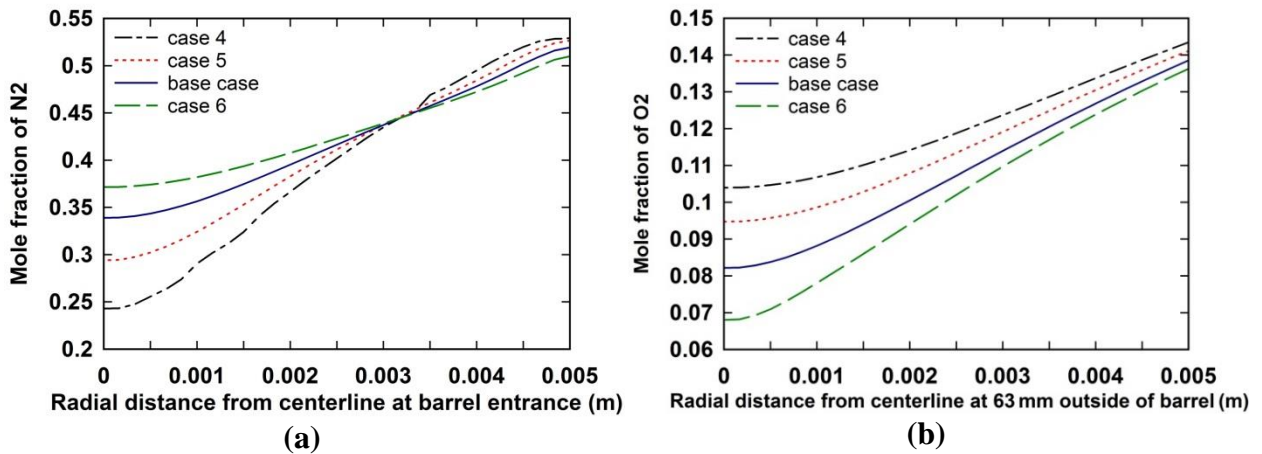


Fig. 14. Effect of throat diameter of the 2nd nozzle on the variation of (a) nitrogen radial distribution at the barrel entrance and (b) oxygen radial distribution at 63mm outside of the barrel (i.e. $x=320$ mm).

478 5.4. Effect of changing the diameters of both converging and C-D nozzles

479 The effects of throat diameters of both converging (1st) and C-D (2nd) nozzles on the gas and
 480 particle dynamic are studied in this section. Fig. 15 presents the velocity and temperature of gas

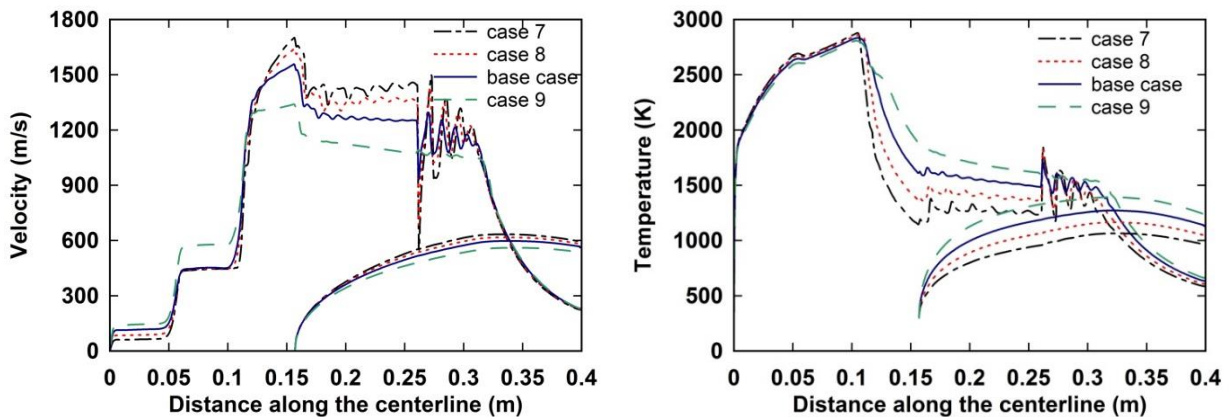
481 and particle phases due to a simultaneous change in the 1st and 2nd nozzle throat diameters.
 482 According to Table 1, for Case 7 and Case 8 the throat diameters of both nozzles are smaller than
 483 the base case while for Case 9 the nozzles have throat diameters higher than the base case. The
 484 results presented in this section show that increasing the diameter of the two nozzles to a same
 485 level, lessens or intensifies the effect of increasing diameter of each nozzle that we observed in the
 486 previous sections.

487 To explain the effect of this geometric modification on particle velocity, we further inspect Figs.
 488 9 (a), 12 (a) and 15 (a). In Fig. 9 (a), it is seen that an increase in the 1st nozzle throat diameter
 489 causes a very slight increase in the velocity (i.e. from 561 m/s to 567 m/s). However, Fig. 12 (a)
 490 shows that an increase in the 2nd nozzle throat diameter results in a noticeable decrease in the
 491 particle velocity (from 600 m/s to 535 m/s). In Fig. 15 (a) it is seen that simultaneous increase of
 492 the 1st and 2nd nozzle throat diameters, decreases the velocity of the particle from 595 m/s to 536
 493 m/s.

494 The velocity ranges given above show that the decrease in the particle velocity of the third
 495 geometrical group (see Table 1) is less severe than the second group. This is because increasing
 496 the first nozzle throat diameter has a slight increasing effect on the particle velocity.

497 This conclusion can also be taken by analyzing the temperature field. Fig. 9 (b) shows that an
 498 increase in the converging nozzle throat diameter increases the particle temperature by 135 K. Fig.
 499 12 (b) also shows that an increase in the C-D nozzle throat diameter increases the particle
 500 temperature by 127 K. In Fig. 15 (b) we can see that simultaneous increase in the both nozzle throat
 501 diameters increases the particle temperature by 274 K. Thus, it is concluded that simultaneous
 502 increase in the both nozzle diameters intensifies separate effects of these changes, and it can
 503 provide us with the particle temperatures twice wider than the range of particle temperature in the
 504 first and second groups of models.

505 Fig. 16 shows the variation of turbulent intensity along the center line due to simultaneous change
 506 of diameters for the 1st and 2nd nozzles. It is seen that increasing the diameters of the two nozzles
 507 (from Case 7 to Case 9 in Table 1) doesn't noticeably affect the turbulent intensity in the
 508 combustion chamber, converging nozzle and mixing chamber (i.e. $0 < x < 0.105$ m). On the other
 509 hand, in the convergent section of the C-D nozzle the turbulence level is more for Case 7.
 510 Therefore, as it can be seen in Fig. 17 (a) the radial distribution of nitrogen and consequently
 511 temperature in the barrel is more uniform in Case 7.



(a) (b)

Fig. 15. Effect of changing throat diameter of both 1st and 2nd nozzles on the variation of (a) velocities and (b) temperatures of the gas and particle phases along the centerline.

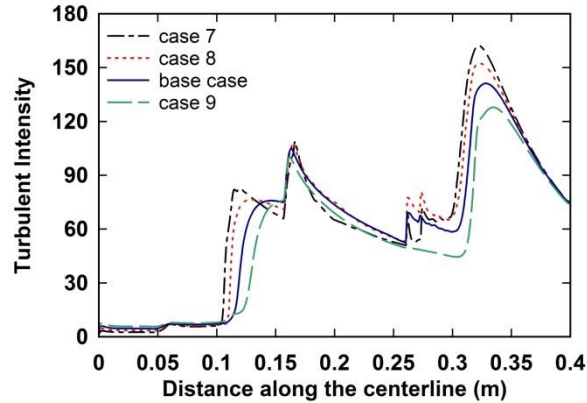


Fig. 16. Effect of changing throat diameter of both 1st and 2nd nozzles on the variation of flow turbulent intensity along the centerline.

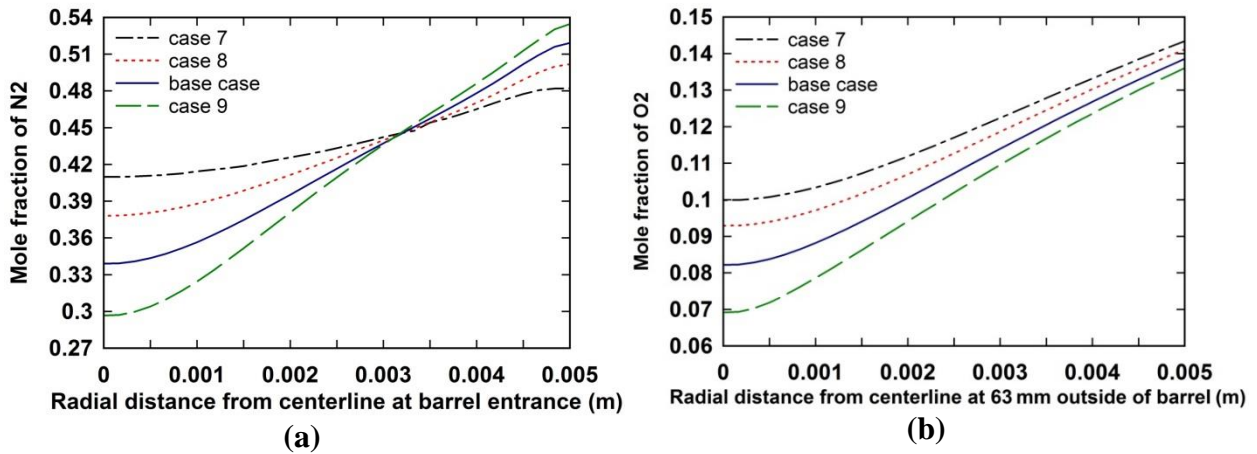


Fig. 17. Effect of changing throat diameter of both 1st and 2nd nozzles on the variation of (a) nitrogen radial distribution at barrel entrance and (b) oxygen radial distribution at 63mm outside of the barrel (i.e. $x = 320$ mm).

512 Fig. 17 (b) also shows the effects of this geometrical change on the radial distribution of oxygen
513 outside the barrel. The results of oxygen mole fraction and turbulent mixing outside the barrel
514 roughly follow what is discussed in the previous parts.

515 5.5. Effect of the length of divergent section in the C-D nozzle

516 In this section we study the effect of the length (L) of the divergent section of the C-D nozzle on
517 the velocity, temperature and turbulent intensity of the two phases. With a fixed divergent angle,
518 a longer divergent section of the C-D nozzle gives the gas phase a chance to reach a lower pressure
519 and temperature and consequently higher velocity when it enters the barrel. Fig. 18 shows the
520 variations of the gas and particle velocity and temperature for different lengths of the divergent
521 section. For Case 10 which the divergent section length is $L = 30$ mm, the flow expands normally
522 to around 1 bar through the C-D nozzle and barrel. Thus, no shock wave is observed at the barrel
523 exit. In contrast, in Case 13 with $L = 50$ mm, the flow over-expands in the C-D nozzle and sharpest
524 series of oblique shocks occur. Fig. 18 (a) shows that while the gas velocity in Case 13 is higher

525 than the other cases, the particle velocity of Case 13 is not more than other cases. The reason is
 526 that in this case the flow expands more through a longer divergent section, and the density of the
 527 flow and consequently the drag force of the flow acting on the particles decreases. This
 528 compensates the effect of higher gas velocity. Fig. 18 (b) shows that as the nozzle length increases,
 529 the flow temperature in the C-D nozzle decreases. Therefore, Case 13 in Fig. 18 (b) yields the
 530 minimum temperature among different cases. Thus, the gas temperature and consequently the
 531 particle temperature is lower than other cases in the barrel. Based on Fig. 18 (b), 40% decrease in
 532 L (comparison between Case 10 and Case 13) does not have significant effect on the temperatures
 533 of the particle and gas phases at the end of the computational domain.

534 Fig. 19 reveals the turbulent intensity of the flow on the centerline for cases 10 to 13. In Case 13,
 535 flow experiences higher speed and stronger shocks at barrel entrance, resulting in more strong
 536 stepwise increase in the turbulent intensity and mixing at the barrel entrance. Thus, as it is seen in
 537 Fig. 20 (a), the radial distribution of nitrogen at the barrel entrance is more uniform in Case 13.
 538 Fig. 20 (b) shows the radial concentration of the oxygen 63 mm outside of the barrel (i.e. $x = 320$
 539 mm in Fig. 3). Roughly same gas phase velocity at the barrel exit leads to same oxygen content at
 540 this section.

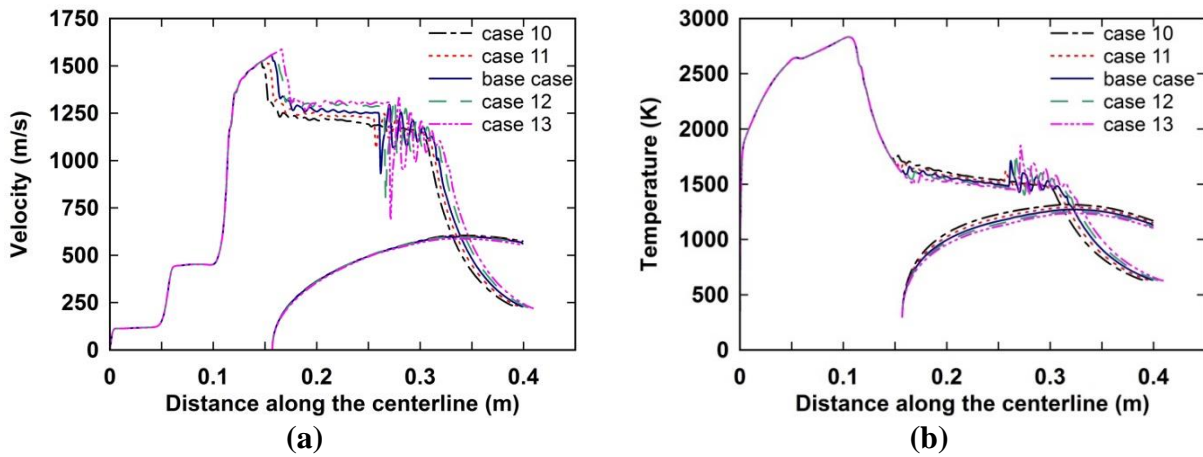


Fig. 18. Effect of divergent section of the C-D nozzle on the variation of (a) velocities and (b) temperatures of the gas and particle phases along the centerline. For better comparison the places of particle injection in all case are shifted to place of base case injection.

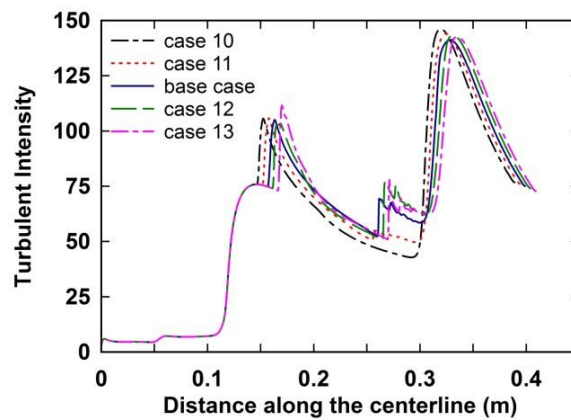


Fig. 19. Effect of divergent section of the C-D nozzle on the variation of turbulent intensity of flow along the centerline.

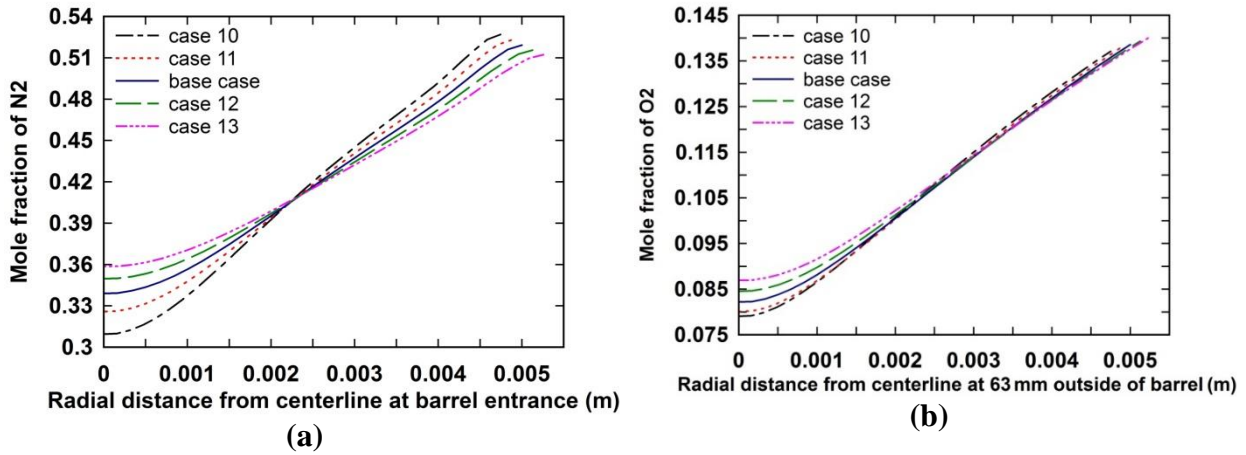


Fig. 20. Effect of divergent section of the C-D nozzle on the variation of (a) nitrogen radial distribution at the barrel entrance and (b) oxygen radial distribution at 63mm outside of the barrel (i.e. $x = 320$ mm).

541

542

543 6. Conclusions

544 Considering the two-way interaction between gas and particle phases, we conducted a parametric
 545 study to investigate the effects of four geometric variables in a dual-stage HVOF thermal spray
 546 gun. The emphasis was placed on the effect of the first and second nozzles geometrical parameters
 547 on the physical properties such as velocity and temperature of the gas and particle phases. The
 548 major findings are as follows:

- 549 • Decouple modeling of the particle and the continuous phase causes a significant error in
 550 predicting the velocity of particle at the impact moment, even for low particle loads.
- 551 • In the first group, decreasing the first nozzle throat diameter results in higher turbulent
 552 mixing in the mixing chamber and C-D nozzle. It helps to achieve more uniform radial
 553 temperature in the barrel. This change does not affect the particle velocity and decreases
 554 the particle temperature. Hence, it can be considered as a way of controlling the particle
 555 temperature at a fixed velocity.
- 556 • In the second group, decreasing the C-D nozzle throat diameter reduces the particle
 557 temperature and increases its velocity. Moreover, it increases the oxygen content of the
 558 free jet outside of barrel and augments the risk of particle oxidation.
- 559 • In the third group, when the diameters of both nozzles are changed, the widest variety of
 560 particle temperature is achieved while the particle velocity remains roughly similar to those
 561 obtained for the second group.
- 562 • By increasing the length of the divergent section of C-D nozzle, the particle velocity does
 563 not change. Therefore, this geometrical parameter can be taken as a way of controlling
 564 particle temperature by preserving its velocity.

565 Funding sources

566 This research did not receive any specific grant from funding agencies in the public, commercial,
567 or not-for-profit sectors.

568 **Reference**

- 569 [1] D.M. Brunette, P. Tengvall, M. Textor, P. Thomsen. Titanium in Medicine: Material Science,
570 Surface Science, Engineering, Biological Responses and Medical Applications, Springer, 2001.
- 571 [2] O.E. Pohler. Unalloyed titanium for implants in bone surgery, *Injury*, 2000, 31, p. 7–13.
- 572 [3] H. Tabbara, S. Gu, D.G. McCartney. Computational modeling of titanium particles in warm
573 spray, *Computers & Fluids*, 2011, 44, p. 358-368.
- 574 [4] R.R. Boyer. An overview on the use of titanium in the aerospace industry, *Materials Science*
575 *and Engineering: A*, 1996, 213, p. 103-114.
- 576 [5] L. Pawlowski. *The Science and Engineering of Thermal Spray Coatings*, 2nd ed., Wiley, 2008.
- 577 [6] M.J. Donachie. *Titanium: a technical guide*, 2nd ed., ASM International, 2000.
- 578 [7] T. Bernecki. Surface science. In: J.R. Davis, editor. *Handbook of Thermal Spray Technology*,
579 1st print, ASM International, 2004, p. 14-35.
- 580 [8] P.L. Fauchais, J.V.R. Heberlein, M.I. Boulos. *Thermal Spray Fundamentals: From Powder to*
581 *Part*, 1st print, Springer, 2014.
- 582 [9] S. Kuroda, J. Kawakita, M. Watanabe, K.H. Kim, R. Molak, H. Katanoda. Current Status and
583 Future Prospects of Warm Spray Technology. In: N. Espallargas, editor. *Future Development of*
584 *Thermal Spray Coatings: Types, Designs, Manufacture and Applications*, 1st ed., Woodhead
585 Publishing, 2015, p. 163-206.
- 586 [10] A. Dolatabadi, J. Mostaghimi, V. Pershin. Effect of a cylindrical shroud on particle conditions
587 in high velocity oxy-fuel (HVOF) spray process, *Journal of Materials Processing Technology*,
588 2002, 137, p. 214-224.
- 589 [11] T. Shamim, C. Xia, P. Mohanty. Modeling and analysis of combustion assisted thermal spray
590 processes, *International Journal of Thermal Sciences*, 2007, 46, p. 755-767.
- 591 [12] C. Ponticaud, A. Grimaud, A. Denoirjean, P. Lefort, P. Fauchais. *Thermal spray 2001: New*
592 *surfaces for a new millennium*, *Proceedings of the International Thermal Spray Conferences*,
593 Singapore, 2001.
- 594 [13] T. Wu, S. Kuroda, J. Kawakita, H. Katanoda, R. Reed. Processing and properties of titanium
595 produced by warm spraying, *Proceedings of the 2006 International Thermal Spray Conference*,
596 Seattle, Washington, USA, 2006.
- 597 [14] M. Watanabe, C. Brauns, M. Komatsu, S. Kuroda, F. Gärtner, T. Klassen, H. Katanoda.
598 Effect of nitrogen flow rate on microstructures and mechanical properties of metallic coatings by
599 warm spray deposition, *Surface & Coatings Technology*, 2013, 232, p. 587-599.

- 600 [15] A. Papyrin, V. Kosarev, S. Klinkov, A. Alkhimov, V.M. Fomin. Cold Spray Technology, 1st
601 ed., Elsevier Science, 2007.
- 602 [16] M.N. Khan, T. Shamim. Effect of operating parameters on a dual-stage high velocity oxygen
603 fuel thermal spray system, Journal of Thermal Spray Technology, 2014, 23, p. 910-918.
- 604 [17] J. Browning, Thermal spray method and apparatus for optimizing flame jet temperature, US
605 patent 5330798 A.
- 606 [18] J. Kawakita, S. Kuroda, T. Fukushima, H. Katanoda, K. Matsuo, H. Fukanuma. Dense
607 titanium coatings by modified HVOF spraying, Surface & Coatings Technology, 2006, 201, p.
608 1250-1255.
- 609 [19] S. Kuroda, J. Kawakita, M. Watanabe, H. Katanoda. Warm spraying-A novel coating process
610 based on high-velocity impact of solid particles, Science and Technology of Advanced Materials,
611 2008, 9, p. 1-17.
- 612 [20] H. Katanoda, T. Kiriaki, T. Tachibanaki, J. Kawakita, S. Kuroda, M. Fukuhara. Mathematical
613 modeling and experimental validation of the warm spray (two-stage HVOF) process, Journal of
614 Thermal Spray Technology, 2009, 18, p. 401-410.
- 615 [21] H. Katanoda, H. Morita, M. Komatsu, S. Kuroda. Experimental and numerical evaluation of
616 the performance of supersonic two-stage high-velocity oxy-fuel thermal spray (warm spray) gun,
617 Journal of Thermal Science, 2011, 20, p. 88-92.
- 618 [22] D. Cheng, Q. Xu, G. Tapaga, E. Lavernia. A numerical study of high-velocity oxygen fuel
619 thermal spraying process. Part I: Gas phase dynamics, Metallurgical and Materials Transactions
620 A, 2001, 32, p. 1609-1620.
- 621 [23] M. Li and P.D. Christofides. Modeling and control of high-velocity oxygen-fuel (HVOF)
622 thermal spray: a tutorial review, Journal of Thermal Spray Technology, 2009, 18, p. 753-768.
- 623 [24] J. Mostaghimi, S. Chandra, R. Ghafouri-Azar, A. Dolatabadi. Modeling thermal spray
624 coating processes: A powerful tool in design and optimization, Surface & Coatings Technology,
625 2003, 163-164, p. 1-11.
- 626 [25] E. Dongmo, M. Wenzelburger, R. Gadow. Analysis and optimization of the HVOF process
627 by combined experimental and numerical approaches, Surface & Coatings Technology, 2008, 202,
628 p. 4470-4478.
- 629 [26] J.S Baik, Y.J Kim. Effect of nozzle shape on the performance of high velocity oxygen-fuel
630 thermal spray system, Surface & Coatings Technology, 2008, 202, p. 5457-5462.
- 631 [27] M. Li, P.D. Christofides. Modeling and analysis of HVOF thermal spray process accounting
632 for powder size distribution, Chemical Engineering Science, 2003, 58, p. 849-857.
- 633 [28] M. Li, P.D. Christofides. Multi-scale modeling and analysis of an industrial HVOF thermal
634 spray process, Chemical Engineering Science, 2005, 60, p. 3649-3669.

- 635 [29] M. Li and P.D. Christofides. Feedback control of HVOF thermal spray process accounting
636 for Powder size distribution, *Journal of Thermal Spray Technology*, 2004, 13, p. 108-120.
- 637 [30] M.N. Khan, T. Shamim. Investigation of a dual-stage high velocity oxygen fuel thermal spray
638 system, *Applied Energy*, 2014, 130, p. 853-862.
- 639 [31] M.N. Khan, T. Shamim. Effect of particle and injection parameters on the performance of a
640 dual-stage high-velocity oxygen fuel thermal spray system, *Journal of Thermal Spray Technology*,
641 2015, 24, p. 807-816.
- 642 [32] V. Yakhot, S. A. Orszag. Renormalization group analysis of turbulence. I. Basic theory,
643 *Journal of Scientific Computing*, 1986, 1, p. 1-51.
- 644 [33] Fluent 6.3, Users Guide, Fluent Inc., 2006.
- 645 [34] B.F. Magnussen, B.H. Hjertager. On the mathematical modeling of turbulent combustion with
646 special emphasis on soot formation and combustion, *Proceedings of the Combustion Institute*,
647 1976, 16, p. 719-729.
- 648 [35] S. Kamnis, S. Gu. 3-D modelling of kerosene-fuelled HVOF thermal spray gun, *Chemical*
649 *Engineering Science*, 2006, 61, p. 5427-5439.
- 650 [36] S. Kamnis, S. Gu. Numerical modelling of propane combustion in a high velocity oxygen-
651 fuel thermal spray gun, *Chemical Engineering and Processing*, 2006, 45, p. 246-253.
- 652 [37] D.B. Spalding. Mixing and chemical reaction in steady confined turbulent flames,
653 *Proceedings of the Combustion Institute*, 1971, 13, p. 649-657.
- 654 [38] T. Poinso, D. Veynante. *Theoretical and Numerical Combustion*, 2nd ed., R.T. Edwards Inc.,
655 2005.
- 656 [39] B.F. Magnussen. On the structure of turbulent and a generalized eddy dissipation concept for
657 chemical reaction in turbulent flow, 19th American Institute of Aeronautics and Astronautics
658 Aerospace Science Meeting, Missouri, USA, January 12-15, 1981.
- 659 [40] J. Chomiak, A. Karlsson. Flame liftoff in diesel sprays, *Proceedings of the Combustion*
660 *Institute*, 1996, 26, p. 2557-2564.
- 661 [41] S. Gordon, B.J. McBride. Computer program for calculation of complex chemical equilibrium
662 compositions and applications, NASA Reference Publication 1311, Cleveland, USA: Lewis
663 Research Center, 1994.
- 664 [42] X. Yang, S. Eidelman. Numerical analysis of a high-velocity oxygen-fuel thermal spray
665 system, *Journal of Thermal Spray Technology*, 1996, 5, p. 175-184.
- 666 [43] D. Cheng, Q. Xu, E. Lavernia, G. Tapaga. The effect of particle size and morphology on the
667 in-flight behavior of particles during high velocity oxy-fuel thermal spraying, *Metallurgical and*
668 *Materials Transactions B*, 2001, 32, p. 525-535.

- 669 [44] W.E. Ranz, W.R. Marshall. Evaporation from drops (Part I), Chemical Engineering Progress,
670 1952, 48, p. 141-180.
- 671 [45] H.K. Versteeg, W. Malalasekera. An Introduction to Computational Fluid Dynamics, 2nded,
672 Prentice Hall, Loughborough, 2007.
- 673 [46] J.D. Anderson. Modern Compressible Flow: with Historical Perspective, 3rd ed., McGraw-
674 Hill Education, 2002.
- 675 [47] H. Tabbara, S. Gu. Computational simulation of liquid-fuelled HVOF thermal spraying,
676 Surface & Coatings Technology, 2009, 204, p. 676-684.